Corrected Copy

IN-02-TM
067623

AIAA 98–0869

Computational/Experimental Aeroheating Predictions for X-33 Phase II Vehicle

H. Harris Hamilton II, K. James Weilmuenster, Thomas J. Horvath, and Scott A. Berry

NASA Langley Research Center, Hampton, VA 23681

36th AIAA Aerospace Sciences Meeting and Exhibit January 12–15, 1998/Reno, NV

Computational/Experimental Aeroheating Predictions for X-33 Phase II Vehicle

H. Harris Hamilton II, K. James Weilmuenster, *
Thomas J. Horvath, and Scott A. Berry †
NASA Langley Research Center, Hampton, VA 23681

Laminar and turbulent heating-rate calculations from an "engineering" code and laminar calculations from a "benchmark" Navier-Stokes code are compared with experimental wind-tunnel data obtained on several candidate configurations for the X-33 Phase II flight vehicle. The experimental data were obtained at a Mach number of 6 and a freestream Reynolds number ranging from 1 to 8 x 10^6/ft. Comparisons are presented along the windward symmetry plane and in a circumferential direction around the body at several axial stations at angles of attack from 20 to 40 deg. The experimental results include both laminar and turbulent flow. For the highest angle of attack some of the measured heating data exhibited a "non-laminar" behavior which caused the heating to increase above the laminar level long before "classical" transition to turbulent flow was observed. This trend was not observed at the lower angles of attack. When the flow was laminar, both codes predicted the heating along the windward symmetry plane reasonably well but under-predicted the heating in the chine region. When the flow was turbulent the LATCH code accurately predicted the measured heating rates. Both codes were used to calculate heating rates over the X-33 vehicle at the peak heating point on the design trajectory and they were found to be in very good agreement over most of the vehicle windward surface.

Nomenclature

Alt	altitude, ft
h	heat transfer coefficient, $BTU-sec/ft^4$
H	enthalpy, ft^2/sec^2
L	vehicle length, *inches*
M	Mach number
p	pressure, lb/ft^2
Re_L	Reynolds number based on length
R_n	nose radius, *inches*
q	heat transfer rate, BTU/ft^2-sec
T	temperature, $degF$
V	velocity, ft/sec
x, y, z	Cartesian body coordinates, *inches*
α	angle of attack, deg
ϵ	surface emissivity
ρ	density, $slugs/ft^3$

Subscripts

FR	Fay and Riddell
w	Wall
∞	Freestream

Introduction

THE Access to Space Study[1] by NASA recommended the development of a heavy-lift *fully* reusable launch vehicle (RLV)[2,3] to provide a next-generation reusable launch system capable of reliably serving national space transportation needs at greatly reduced cost. As part of this program, the X-33 serves as a technology demonstrator for the RLV. It is envisioned to be approximately a one-half-scale prototype of the RLV that will demonstrate the technologies required to develop and operate a full scale vehicle.

At the completion of a X-33 Phase I competition, Lockheed Martin Skunk Works was awarded the Phase II contract for the design, development and construction of the X-33 flight vehicle. In addition, Lockheed is in charge of the flight test program. It is an industry led effort in *partnership* with NASA to support the design and development work on the X-33 through formal task agreements.

In the design of any hypersonic vehicle, aerodynamic heating is an important issue. This paper presents results generated in support of task agreements with Lockheed to provide experimental aerodynamic heating data and computational fluid dynamic (CFD) calculations in support of X-33 aerothermodynamic development and design.[4] It should be viewed as a report of *work-in-progress* since additional work will be performed during the next several months that will also support the final design.

Results from experimental heating measurements and CFD computations are presented and compared. In addition, ongoing efforts in support of these task agreements will be discussed. Some of the experimental heating results presented in this paper were in support of the task to study laminar-to-turbulent boundary-layer transition.[5]

*Senior Research Engineer, Aerothermodynamics Branch, Aero- and Gas-Dynamics Division, Research and Technology Group, Associate Fellow AIAA.

†Research Engineer, Aerothermodynamics Branch, Aero- and Gas-Dynamics Division, Research and Technology Group.

X-33 Geometry

The X-33 configuration is a lifting body design with symmetrical canted fins, twin vertical tails, and two body flaps located at the rear of the fuselage. The vehicle is powered by a linear Aero-spike engine. It has a length of approximately 756 inches from the nose to the end of the engine block and a span of approximately 920 inches from wing tip to wing tip. The geometry of the X-33 vehicle has evolved during the course of both the Phase I and II efforts,[4] thus results from several different vehicle geometries (D Loft, Rev C, and Rev F) are discussed in this paper. The D Loft was the configuration that emerged from Phase I and was used in the early part of Phase II.

The Rev C configuration is a revision of the D-loft. For Rev-C, the nose region had a slightly different shape to simplify the construction of the metallic panels used in the Thermal Protection System (TPS) and there were also changes in the base region. Both a top and bottom perspective view of this configuration are shown in Figs. 1 and 2, respectively.

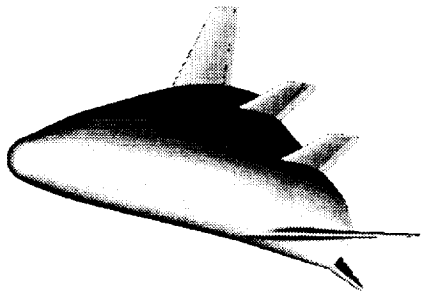

Fig. 1 Top view of X-33 Rev–C configuration

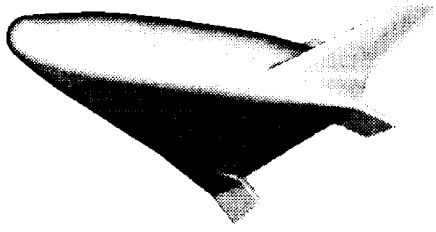

Fig. 2 Bottom view of X-33 Rev–C configuration

The dihedral of the canted-fin on both the D–Loft and Rev C configurations was 37 degrees.

The Rev F is a further revision of the vehicle geometry to improve its aerodynamic characteristics. This configuration has the same forebody shape as Rev C but the dihedral of the canted fin was lowered to 20 degrees to improve pitch-trim characteristics across the speed range and the size of the leeside vertical tails was increased to improve lateral-directional stability at low speeds. Although there have been additional vehicle modifications since Rev F, these modifications have been relatively minor.

Experimental Method and Test Conditions

Experimental results presented in this paper were obtained in the NASA Langley Research Center (LaRC) 20-Inch Mach 6 Tunnel. The tunnel is a hypersonic blow down facility which uses heated, dried, filtered air as the test medium. Typical operating conditions for this tunnel cover a range of stagnation pressures from 30 to 500 psi, stagnation temperatures from 760° R to 1000° R, and freestream unit Reynolds numbers from approximately 0.5 to 8 x 10^6 per foot. For these operating conditions, the freestream Mach number ranges between approximately 5.8 and 6.1. The tunnel has a two-dimensional nozzle and a test section that is 20.5 by 20 inches. A more detailed description of the facility is given by Micol.[6]

Experimental heating tests were conducted on a 10-inch forebody of the D Loft configuration, representing approximately the forward 70 percent of the full vehicle, and on a Rev–C, 10-inch "tip-to-tail" configuration in the Langley 20-Inch Mach 6 Tunnel. The tests on the D–Loft forebody model were part of a study designed to obtain "smooth body or natural" boundary-layer transition on the X-33 vehicle.[5] Because of the fast paced nature of the X-33 program, the models used in the experimental tests presented in this paper were not measured to determine how well they agreed with the vehicle shape. However, for all future experimental heating models, quality assurance measurements are planned as a part of the model construction process.

The experimental test conditions for these experiments are given in Tables 1 and 2, respectively. Two identical models (designated A and B) were used during the D Loft forebody tests to look at the effect of model construction on both the heat transfer and transition results.

All the heat transfer measurements were performed using a two-color, relative-intensity phosphor thermography technique to enable optical acquisition of the test data.[7,8] With this technique, silica ceramic wind-tunnel models are slip casted[9] and coated with a mixture of phosphors which fluoresce in two regions of the visible spectrum (red and green) when illuminated with ultraviolet light. The fluorescence intensity is dependent on the amount of incident light and local temperature of the phosphors. By acquiring

Table 1 Test conditions for D–Loft forebody.

Run	Model	M_∞	α deg	p_∞ lb/ft^2	T_∞ deg R	Re_L x 10^{-6}
6	A	5.95	40	12.22	112.9	1.86
8	A	5.97	40	23.77	111.8	3.70
24	B	5.97	40	23.60	111.7	3.67
7	A	5.99	40	33.79	114.6	5.07
32	B	5.99	40	33.75	115.5	4.99
9	A	6.00	40	43.04	112.7	6.64
15	A	5.99	30	33.79	114.6	5.07
19	A	5.98	20	33.52	114.1	5.06
30	B	5.98	20	34.04	115.4	5.03

Table 2 Test conditions for Rev–C configuration.

Run	M_∞	α deg	p_∞ lb/ft^2	T_∞ deg R	Re_L x 10^{-6}
6	5.96	30	5.76	109.4	0.93
5	5.97	30	11.80	112.0	1.83
4	5.99	30	23.35	111.8	3.64
7	6.00	30	33.56	114.5	5.05
31	5.99	20	23.04	111.1	3.63
2	5.99	40	23.29	111.4	3.65

fluorescence intensity images of an illuminated model exposed to the wind-tunnel flow, surface temperature maps can be calculated on portions of the model in the camera's view. A temperature calibration of the system conducted prior to the test provides data necessary to convert the two-color images to temperature. Acquiring images (temperatures) at different times in the wind-tunnel run enables local heat transfer coefficient to be computed. Comparison of heat transfer measurements obtained with the thermographic phosphor technique to those obtained using conventional thin-film resistance gauges have shown excellent agreement.[10]

In routine use of this technique, the phosphor coating (≈1 mil in thickness) has proven robust and does not typically require refurbishment during a test. This technique, which has been widely used at the Langley Research Center, offers two distinct advantages over conventional heat transfer test methods. First, the measurements provide a quantitative resolution of global surface temperatures and heating unlike discrete gauge measurements. In addition, the model construction, testing and data reduction can be performed much faster and cheaper than other testing methods.

Computational Methods

Experimentally measured heating data are compared with predictions from a "benchmark" Navier-Stokes code (LAURA – Langley Aerothermodynamic Upwind Relaxation Algorithm), and an "engineering" code (LATCH – Langley Approximate Three-Dimensional Convective Heating), which is based on a boundary-layer-inviscid method.

LAURA Code

The LAURA code[11–13] is a three-dimensional, finite-volume, Navier-Stokes code based on an upwind relaxation algorithm that can compute both perfect and real gas flows. Inviscid fluxes are computed using Roe's averaging[14] and Yee's[15] Symmetric Total Variation Diminishing (STVD) to achieve second order accuracy away from discontinuities. Second order accurate, central differences are used to compute the viscous flux.

The governing equations are solved by marching in "pseudo" time until a steady state solution is achieved. The treatment of the governing equations is described as point implicit because variables at the cell center are treated implicitly, whereas the latest available data are used for the other terms. With this strategy, updating cell centered variables requires the inversion of a much smaller matrix and only one level of storage. The LAURA code has been shown to compare well with both flight[16] and wind tunnel[17] data.

LATCH Code

The LATCH code[18,19] is an approximate three-dimensional heating code based on the axisymmetric analog for general three-dimensional boundary layers.[20] In this method the boundary-layer equations are first written in a streamline-oriented coordinate system (s, β, n) where s is the distance measured along an inviscid streamline, β is tangent to the surface and normal to the streamline direction, and n is normal to the surface. If the viscous crossflow in the boundary layer is small and can be neglected (as it can be when the streamline curvature is small or when the wall is cold), the boundary-layer equations reduce to an axisymmetric form if s is interpreted as the distance along an "equivalent" axisymmetric body and the metric coefficient h, associated with the spreading of the streamlines, is interpreted as the radius of the equivalent axisymmetric body. This greatly simplifies the boundary-layer solution and means that approximate three-dimensional heating rates can be computed along an individual streamline independent of other streamlines using any axisymmetric heating prediction method. The approach is simplified further by using an approximate integral heating technique,[21] which has been shown to agree with more detailed finite-difference boundary-layer solutions, to calculate heating rates. In practice, solutions are carried out along multiple streamlines simultaneously in a marching fashion so that the approximate boundary solution over the complete body is obtained in a single pass down the body requiring about 5 10 minutes on a desktop workstation.

To apply this method, the inviscid streamlines

and metric coefficients are required and must be obtained from a three-dimensional inviscid solution. In this paper the inviscid solutions were obtained using the inviscid version of the LAURA code, described previously, and the inviscid version of the DPLUR code,[22] a flowfield code that has been optimized for running on parallel computers. These solutions require more time than the LATCH boundary-layer solutions, but much less time than the full Navier-Stokes solutions. The primary advantage of the LATCH code is that reasonably accurate heating solutions can be obtained in much less time than for a Navier-Stokes code and thus more solutions can be computed for the same expenditure of resources. The relatively fast turnaround makes LATCH an extremely useful code for vehicle design. The LATCH code has been shown to compare well with both wind tunnel and flight data and with other more detailed flowfield codes.[19,23]

All of the calculations for wind tunnel conditions presented in this paper for both the LAURA and LATCH codes were run for a constant wall temperature of 540 deg. R (80 deg. F). The heating data for these conditions are presented in terms of heat transfer coefficient to minimize the effect of wall temperature on the results. The flight calculations were run at the local radiation equilibrium wall temperature assuming a surface emmisivity of 0.9.

Results and Discussion

In this section, heating predictions from the LATCH and LAURA code are first compared with experimental heating measurements obtained in the 20-Inch Mach 6 Tunnel on a D Loft forebody model and a Rev–C "tip-to-tail" model. Predictions from the LATCH and LAURA codes are then compared for the peak laminar heating point on the X-33 design trajectory.

D–Loft Forebody

As a part of the X-33 boundary-layer transition study,[5] a 10-inch forebody model of the D–Loft configuration (approximately 0.019 scale) was constructed. This model represents approximately the forward 70 percent of the complete configuration from the nose to just ahead of the canted-fin, fuselage juncture (see Figs. 1 and 2). A perspective view of the forebody configuration is shown in Fig. 3. The model size represented a compromise between the desire to test the largest possible model to enhance the probability of obtaining "smooth body or natural" transition over a range of angles of attack ($20^o \leq \alpha \leq 40^o$) and the desire to minimize the disturbance or blockage of the flow in the tunnel.

Although no experimental hypersonic pressure data have been obtained on any of the X-33 configurations, calculated results are available. The calculated surface pressure distributions along the windward symmetry plane are presented in Fig. 4 for $\alpha = 20^o, 30^o$, and 40^o angle of attack. Only the inviscid results are presented since both the inviscid and viscous LAURA calculations are in good agreement. The pressures increase with angle of attack as would be expected. There are two regions of over expansion and recompression: one near $x/L \approx 0.1$, and the second near $x/L \approx 0.45$. The strength of both recompression regions increases with angle of attack. For this Mach number, the nondimensional pressure at the sonic point is approximately 0.49, thus at $\alpha = 20^o$ and 30^o the sonic point is on the nose ahead of the first recompression but at $\alpha = 40^o$ the sonic point is located much further downstream at $x/L \approx 0.35$.

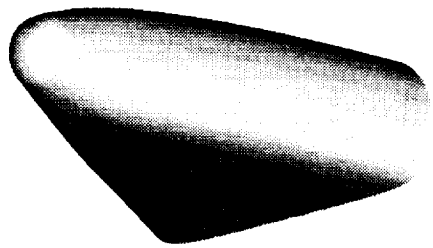

Fig. 3 X-33 D–Loft forebody configuration

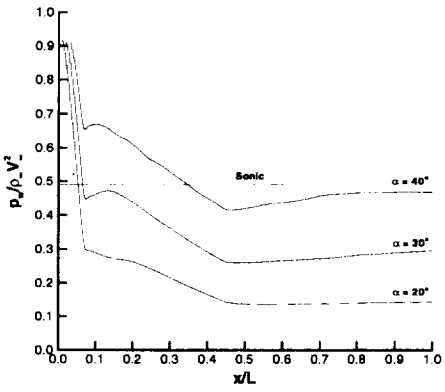

Fig. 4 Windward symmetry plane inviscid pressures on the D–Loft forebody configuration at $M_\infty = 6$.

Inviscid surface streamlines on the lower surface are presented in Figs. 5–7 for $\alpha = 20.^o 30.^o$ and $40.^o$, respectively. At $\alpha = 40,^o$ the pressure on the symmetry plane is higher than for the lower angles of attack and the streamline patterns indicate that there is outflow on the lower surface. However, at $\alpha = 20,^o$ the windward symmetry plane pressure is lower and the streamlne patterns indicate much more inflow than at the higher angles of attack.

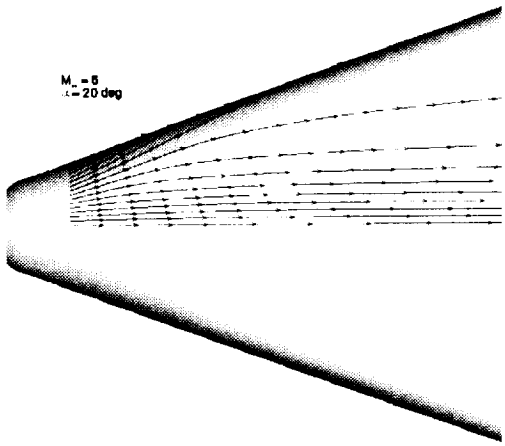

Fig. 5 Inviscid surface streamlines on windward side the D–Loft forebody configuration at $M_\infty = 6$, $\alpha = 20^o$.

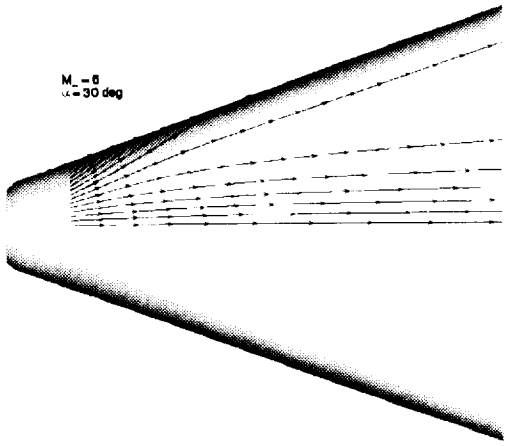

Fig. 6 Inviscid surface streamlines on windward side the D–Loft forebody configuration at $M_\infty = 6$, $\alpha = 30^o$.

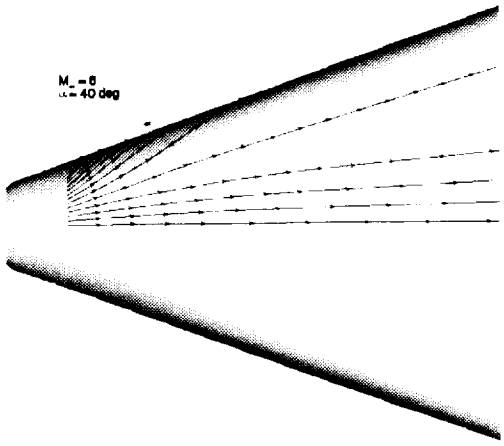

Fig. 7 Inviscid surface streamlines on windward side the D–Loft forebody configuration at $M_\infty = 6$, $\alpha = 40^o$.

Windward symmetry plane heating results at $\alpha = 40^o$ and $Re_L = 1.83x10^6$, are presented in Fig. 8.

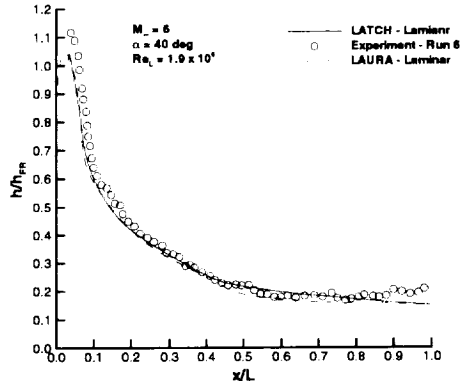

Fig. 8 Windward symmetry heating on the D–Loft forebody at $M_\infty = 6$, $\alpha = 40^o$, and $Re_L = 1.9x10^6$.

The heating results are presented as a heat transfer coefficient ratio h/h_{FR} versus x/L, where h is the local heat transfer coefficient and h_{FR} is the stagnation point heat transfer coefficient calculated using the theory of Fay and Riddell[24] for a sphere with the radius approximately equal to the nose radius of the model ($R_n = 1.033$ inches). Presenting the heat transfer results in this form (i. e. h/h_{FR}) has two benefits. First, the sensitivity of the results to wall temperature variations is essentially removed. This is important for these wind tunnel data because the wall to total enthalpy ratio is relatively high ($h_w/h_{aw} \approx 0.6$) and the measured heating rate is significantly affected by variation in the wall temperature while the heat transfer coefficient is not. For the hypersonic portion of the X-33 flight trajectory the wall to total enthalpy ratio is lower (0.2 0.3) and the effect of wall temperature on heat transfer rate is much lower than for the Mach 6 wind tunnel. The second benefit is that, for the range of Reynolds numbers in the 20-Inch Mach 6 tunnel, this ratio is relatively insensitive to Reynolds number variation for laminar flow because both the numerator and denominator have a similar dependence.

In figure 8, both the LATCH and LAURA calculations are compared with the experimental heating data along the windward symmetry plane for an angle of attack of 40^o and a Reynolds number based on model length of $1.9x10^6$. In both sets of calulations the flow has been assumed to be laminar because of the relatively low Reynolds number for this case. The LAURA predictions are in good agreement with the measured heating over the entire length of the model. The differences are largest in the stagnation region where the measured heating is approximately 10 percent higher than the LAURA prediction but downstream of the stgnation region the LAURA predictions generally agree with the measured heating data within about 5 percent or less. The LATCH predictions are in

good agreement with both the LAURA predicitions and with the measured heating data over the entire length of the model. The good agreement between LATCH and the other results for this case is encouraging.

For this same case, lateral distributions at four axial stations $x/L = 0.3, 0.5, 0.7$, and 0.9 are presented in Figs. 9 12, respectively. The heating results are plotted in the form of h/h_{FR} versus y/L where y is the lateral coordinate on the body which is zero in the symmetry plane and L is the model length ($L = 10$ inches).

At $x/L = 0.3$ (Fig. 9), the heating is a minimum near the symmetry plane ($y/L = 0$) and rises to a peak in the chine region. Both LATCH and LAURA predict an increase in heating in the chine region as would be expected, with LAURA predictions being approximately 10 percent higher than LATCH predictions. However, both are significantly lower than the measured data in this region (25-30 percent). This was not expected since the flow was thought to be laminar at this Reynolds number, and based on experience with other configurations such as the Shuttle Orbiter (which has a much smaller chine radii), it would be expected that the predictions would be in better agreement with laminar data. The LAURA solution was run for a sufficient time to achieve convergence for the grid that was used (161 x 181 x 64). A grid convergence study is planned but has not been completed. However, based on LAURA calculations on other configurations, such as the Shuttle Orbiter, it is thought that the grid is sufficient to produce accurate heating predictions. Similar results are noted for the other lateral heating distributions at $x/L = 0.5, 0.7$, and 0.9 in Figs. 10, 11, and 12.

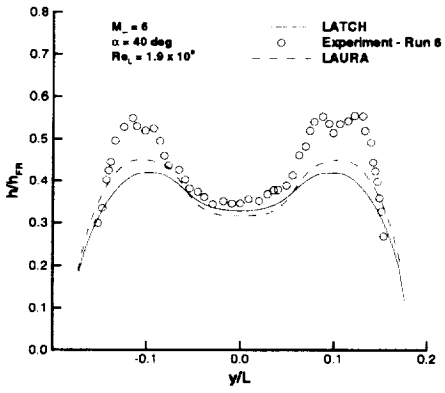

Fig. 9 Lateral heating distribution on the D–Loft forebody at $x/L = 0.3$, $M_\infty = 6$, $\alpha = 40^o$, and $Re_L = 1.9x10^6$.

For this angle of attack ($\alpha = 40^o$), heating distributions along the windward symmetry plane for three higher Reynolds numbers, Re_L = 3.7, 5.0, and 6.6 x $10,^6$ are presented in Figs. 13, 14, and 15. For $Re_L = 3.7x10^6$ (Fig. 13), there is good qualitative

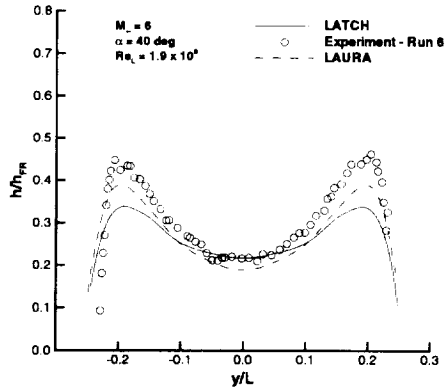

Fig. 10 Lateral heating distribution on the D–Loft forebody at $x/L = 0.5$, $M_\infty = 6$, $\alpha = 40^o$, and $Re_L = 1.9x10^6$.

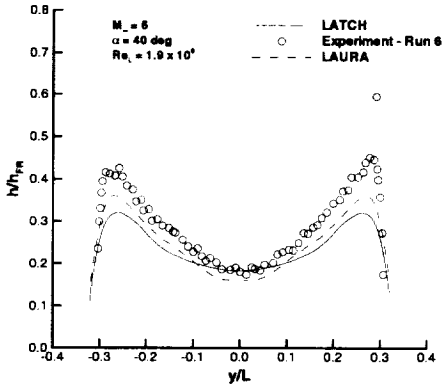

Fig. 11 Lateral heating distribution on the D–Loft forebody at $x/L = 0.7$, $M_\infty = 6$, $\alpha = 40^o$, and $Re_L = 1.9x10^6$.

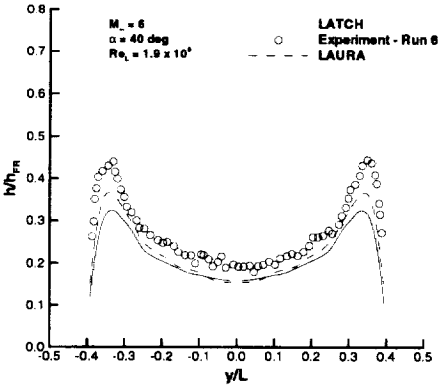

Fig. 12 Lateral heating distribution on the D–Loft forebody at $x/L = 0.9$, $M_\infty = 6$, $\alpha = 40^o$, and $Re_L = 1.9x10^6$.

agreement between the measured heating data and the laminar calculations of both LATCH and LAURA until near x/L $\approx$ 0.6 where the measured heating rises rapidly indicating that boundary layer undergoes transition. The heating continues to rise downstream until it exceeds the turbulent LATCH calculations near the end of the body suggesting that the flow is close to fully turbulent in this region. Experimental data from two different runs have been included in the figure. The two experimental heating results are in reasonably good agreement.

For $Re_L = 5.0x10^6$ (Fig. 14), the measured heating data follows the laminar LATCH calculations to a value of x/L $\approx$ 0.1 where it begins to depart from the prediction. No LAURA calculations are available at this Reynolds number. At x/L $\approx$ 0.5–0.6, the measured heating rises rapidly to a value slightly above the turbulent LATCH prediction and maintains that level until near the end of the body. In general the turbulent LATCH predictions agree with the measured data to within 10–12 percent.

For the highest Reynolds number tested, $Re_L = 6.6x10^6$ (Fig. 15), laminar predictions are available from both LATCH and LAURA. The trend of the experimental and predicted results are similar to those at $Re_L = 5.0x10^6$ (Fig. 14), except that the departure between the measured heating and the predictions near x/L $\approx$ 0.1 is much more apparent. It is interesting to note that the location where the measured heating departs from the laminar predictions is just downstream of the first recompression region observed in the predicted pressure distributions (Fig. 4). It may be possible that this recompression is introducing a disturbance in the flow that causes the heating to depart from the expected laminar trend and eventually builds up and produces the classical "transition" behavior that is observed further down the body. It may also be possible that there is sufficient surface roughness in the nose region to produce a disturbance in the flow that causes the downstream heating to increase above the laminar level until it has grown sufficiently strong to promote the classical transition behavior observed further downstream. A behavior similar to this has been observed by Berry, et al.[25] during tests of discrete surface roughness on the Shuttle Orbiter. Whatever the cause, the heating aft of $x/L \approx 0.1$ does not follow the expected laminar trends. The heating when plotted as h/h_{FR} should remain approximately constant at a fixed location on the model with increasing Reynolds number for laminar flow.. Comparing results for the various Reynolds numbers, Figs. 8 and 13–15, it can be seen that this is the observed behavior for the laminar calculations but it is not for the experimental measurements; thus, there must be some kind of disturbance that is causing the flow to depart from laminar. If this is true it may also be affecting the lateral heating in the chine region that was observed previously at the lower Reynolds number in Figs. 9-12.

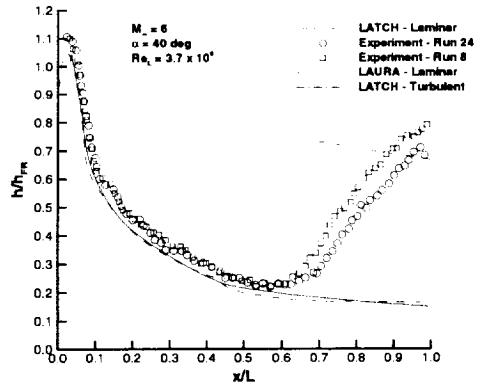

Fig. 13 Windward symmetry heating on the D-Loft forebody at $M_\infty = 6$, $\alpha = 40°$, and $Re_L = 3.7x10^6$.

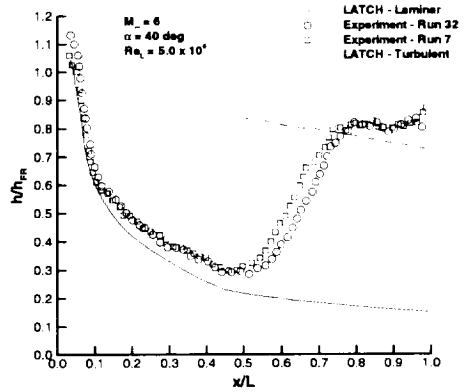

Fig. 14 Windward symmetry heating on the D-Loft forebody at $M_\infty = 6$, $\alpha = 40°$, and $Re_L = 5.0x10^6$.

For the highest Reynolds number case, $Re_L = 6.6x10^6$, lateral distributions at the same four axial stations, $x/L = 0.3$, 0.5, 0.7, and 0.9, as shown previously at a lower Reynolds number are presented in Figs. 16–19. From results presented previously, (see Fig. 15), it was shown that on the windward symmetry plane the measured heating data departed from a laminar behavior downstream of x/L $\approx$ 0.1. A similar behavior in the lateral heating distributions is observed in Figs. 16–19. The difference between measured heating and laminar predictions increases with each successive downstream lateral cut until at $x/L = 0.7$ (Fig. 18), the heating on the center portion of the model agrees with the turbulent LATCH predictions. The spike in heating near y/L $\approx$ -0.2 observed in this cut plane is caused by a small damaged area on the model due to a particle in the flow striking the phosphor coating. This *unintended roughness element* caused localized early boundary transition. At $x/L = 0.9$, the localized transition region caused

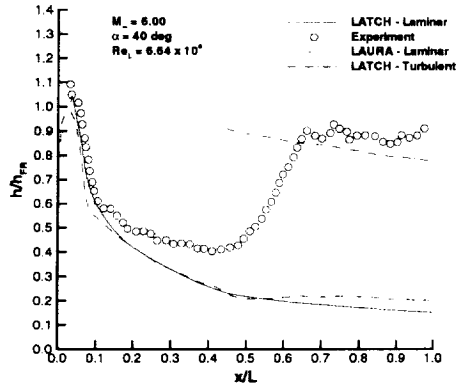

Fig. 15 Windward symmetry heating on the D–Loft forebody at $M_\infty = 6$, $\alpha = 40^o$, and $Re_L = 6.6x10^6$.

by the "trip" has merged with the wedge of turbulent flow over the central portion of the model and the measured data are in good agreement (10 percent) with the LATCH turbulent predictions. In fact, for all cases where the flow was clearly turbulent, the LATCH calculations agree well with the experimental measurements.

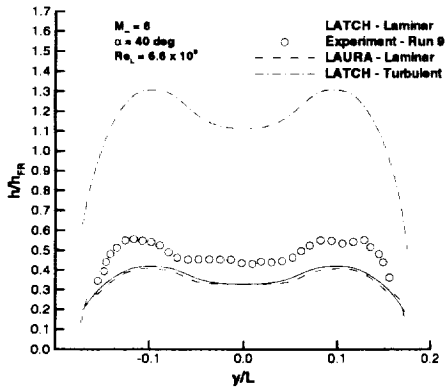

Fig. 16 Lateral heating distribution on the D–Loft forebody at $x/L = 0.3$, $M_\infty = 6$, $\alpha = 40^o$, and $Re_L = 6.6x10^6$.

Finally, for a $Re_L \approx 5x10^6$, windward symmetry plane heating distributions for this configuration are presented for two lower angles of attack ($\alpha = 20^o$ and 30^o) in Figs. 20 and 21.

For $\alpha = 20^o$ (Fig. 20), two sets of data obtained on different models (see Table 2), are included. Both sets of measurements are in excellent agreement with each other and also with laminar heating computed by LATCH. For this case the flow appears to be completely laminar.

At $\alpha = 30^o$ (Fig. 21), the measured heating agrees with the LATCH laminar predictions for $x/L \leq 0.6$ and then rises rapidly, indicative of transition, to a level slightly above the turbulent LATCH prediction. These results (shown in Figs. 20, 21, and 14) graphi-

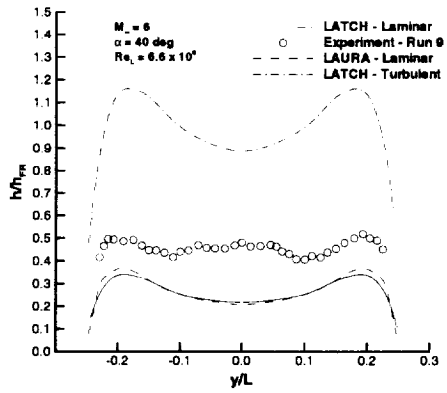

Fig. 17 Lateral heating distribution on the D–Loft forebody at $x/L = 0.5$, $M_\infty = 6$, $\alpha = 40^o$, and $Re_L = 6.6x10^6$.

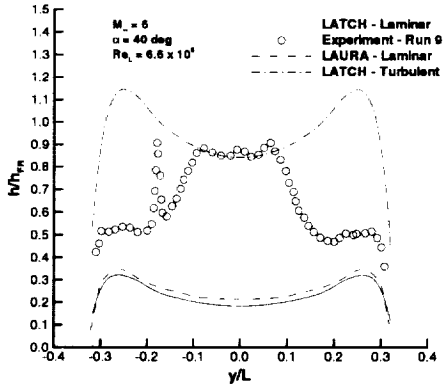

Fig. 18 Lateral heating distribution on the D–Loft forebody at $x/L = 0.7$, $M_\infty = 6$, $\alpha = 40^o$, and $Re_L = 6.6x10^6$.

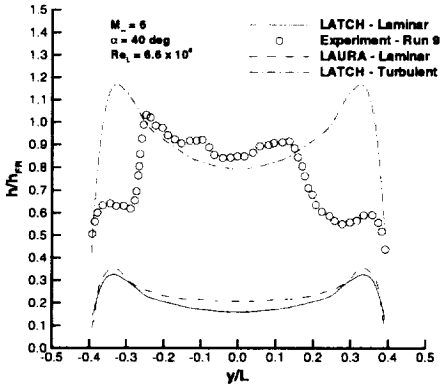

Fig. 19 Lateral heating distribution on the D–Loft forebody at $x/L = 0.9$, $M_\infty = 6$, $\alpha = 40^o$, and $Re_L = 6.6x10^6$.

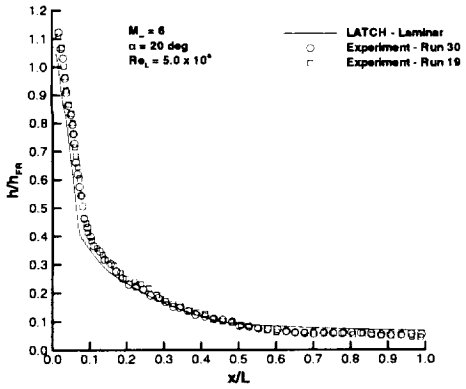

Fig. 20 Windward symmetry heating on the D-Loft forebody at $M_\infty = 6$, $\alpha = 20^o$, and $Re_L = 5.0x10^6$.

cally illustrate the forward movement transition with increasing angle of attack discussed by Thompson, et al.[5]

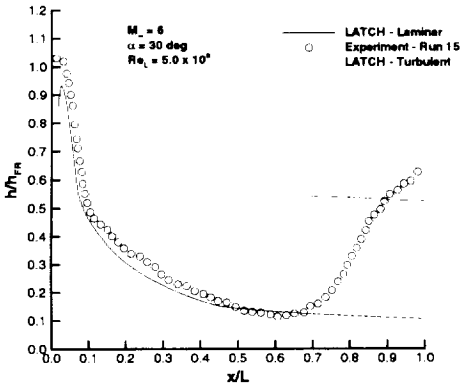

Fig. 21 Windward symmetry heating on the D-Loft forebody at $M_\infty = 6$, $\alpha = 30^o$, and $Re_L = 5.0x10^6$.

Rev-C Configuration

Heat transfer tests have been conducted on a Rev C tip-to-tail model that had a length of 10 inches from the tip of the nose to the end of the engine block (approximately 0.0132 scale). In this section measured heating data from these tests are presented along with predictions from the LATCH code.

First, heating distributions along the windward symmetry plane for $Re_L \approx 3.6x10^6$ and $\alpha = 20^o$, 30^o and 40^o are presented in Figs. 22, 23, and 24, respectively. In general, both the measured heating and the LATCH predictions increase with angle of attack would be expected. However, for all angles of attack, the experimental data are higher than the LATCH calculations in the nose region, x/L $\leq$ 0.3, and somewhat lower for x/L $\geq$ 0.3. The reason for this disagreement is unknown. Although, no LAURA calculations are available for this configuration at these conditions, based on the comparisons between LAURA and LATCH for the D Loft forebody model shown previously and on other comparisons at flight conditions (which will be shown in the next section) LAURA and LATCH would be expected to give similar predictions for this case. However, as pointed out previously, the models have not been tested for quality assurance and differences in shape between the wind tunnel and computational model geometries could cause some of the observed difference between experiment and prediction. For all future X-33 heating tests, quality assurance measurements have been planned as an integral part of the model construction process.

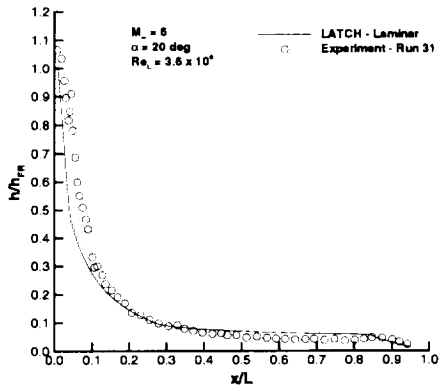

Fig. 22 Windward symmetry plane heating on the Rev-C configuration at $M_\infty = 6$, $\alpha = 20^o$, and $Re_L = 3.6x10^6$.

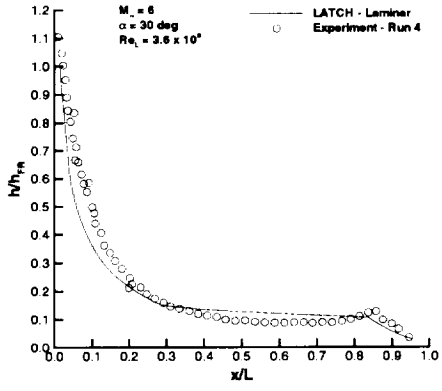

Fig. 23 Windward symmetry plane heating on the Rev-C configuration at $M_\infty = 6$, $\alpha = 30^o$, and $Re_L = 3.6x10^6$.

For $\alpha = 30^o$ and $Re_L = 3.6x10^6$, lateral heating distributions at $x/L = 0.3, 0.5, 0.7, 0.8$, and 0.9 are presented in Figs. 25–29, respectively. The two most forward stations at $x/L = 0.3$ and 0.5 (Figs. 25 and 26) are ahead of the canted-fin, fuselage juncture and the heating distribution is similar to that shown previously for the D Loft forebody model. Both the experimen-

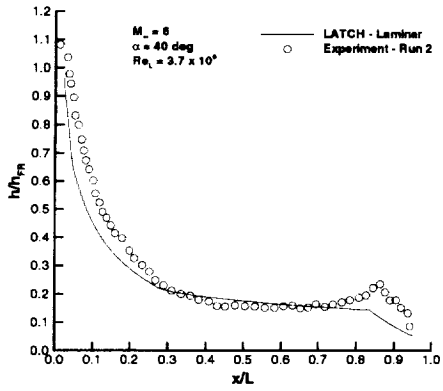

Fig. 24 Windward symmetry plane heating on the Rev–C configuration at $M_\infty = 6$, $\alpha = 40^o$, and $Re_L = 3.6x10^6$.

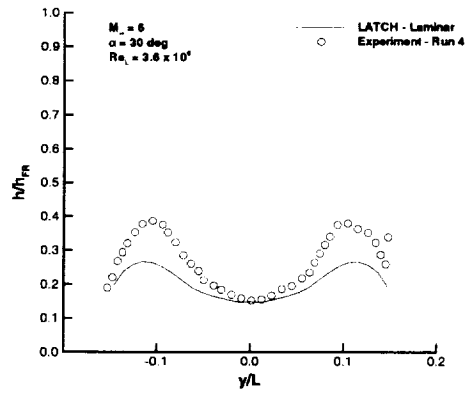

Fig. 25 Lateral heating distribution on the Rev–C configuration at $x/L = 0.3$, $M_\infty = 6$, $\alpha = 30^o$, and $Re_L = 3.6x10^6$.

tal data and the LATCH computations are lowest near the symmetry plane ($y/L = 0$) and increase to a maximum in the chine region. The LATCH predictions are in reasonably good quantitative agreement with the measured heating near the symmetry plane but are significantly lower than the measured data in the chine region. This is similar to the results shown previously for the D–Loft. Additional heating tests are planned for the Rev–F configuration, which is a later version of the X-33 vehicle than those included in this paper. As a part of these tests, extensive supporting calculations are planned to further investigate the consistent trend observed here of underpredicting the "laminar" chine heating.

Further aft on the model, the lateral cuts at $x/L = 0.7, 0.8$ and 0.9 (Figs. 27, 28, and 29) include data on the windward side of the canted fin. For $x/L = 0.7$ (Fig. 27) and 0.8 (Fig. 28), the heating increases in a direction away from the symmetry plane ($y/L = 0$), reaches a peak in the chine region (y/L ≈ 0.2–0.3), decreases around the side of the fuselage, and then increases again on the windward side of the canted fin. The LATCH predictions are in good qualitative agreement with the experimental measurements but again underpredict the heating on the chines. The overall comparison on the windward side of the canted fin is better than on the chines. For $x/L = 0.9$ (Fig. 29), the trends are similar to those at the two previous axial stations ($x/L = 0.7$ and 0.8) but lower heating is observed over the center portion of the model. This lower heating is caused by an expansion region on the rearward portion of the lower surface. The tip of one of the canted was broken off during the expermental tests. This accounts for the asymmetry in the measured heating outboard of the chine region for negative values of y/L at this axial station ($x/L = 0.9$).

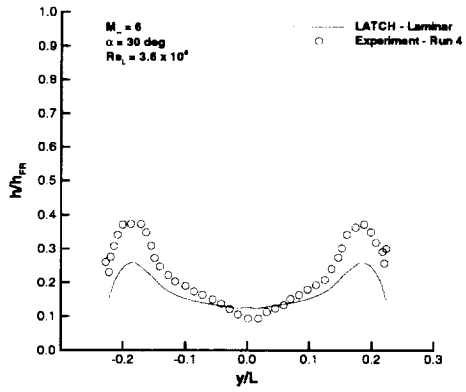

Fig. 26 Lateral heating distribution on the Rev–C configuration at $x/L = 0.5$, $M_\infty = 6$, $\alpha = 30^o$, and $Re_L = 3.6x10^6$.

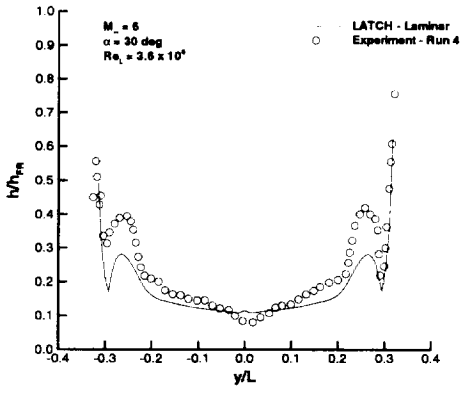

Fig. 27 Lateral heating distribution on the Rev–C configuration at $x/L = 0.7$, $M_\infty = 6$, $\alpha = 30^o$, and $Re_L = 3.6x10^6$.

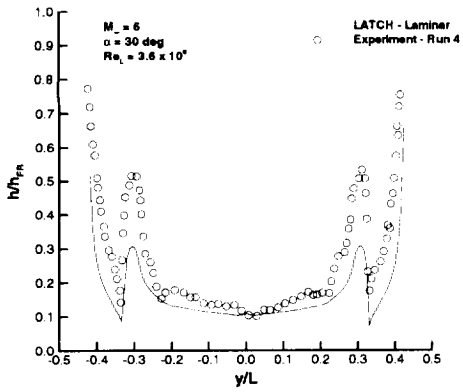

Fig. 28 Lateral heating distribution on the Rev-C configuration at $x/L = 0.8$, $M_\infty = 6$, $\alpha = 30^o$, and $Re_L = 3.6x10^6$.

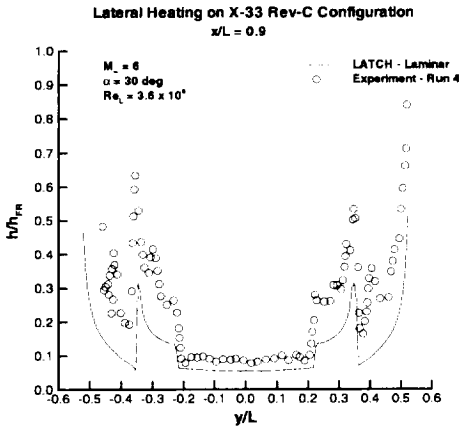

Fig. 29 Lateral heating distribution on the Rev-C configuration at $x/L = 0.9$, $M_\infty = 6$, $\alpha = 30^o$, and $Re_L = 3.6x10^6$.

Flight Predictions

In this section computed heating results from the LATCH code are compared with computed heating results from the LAURA code at the peak laminar heating point on the nominal TPS (Thermal Protection System) design trajectory. The freestream conditions for this case are given in Table 3.

Table 3 Freestream conditions for flight calculations

Altitude	=	175.8	kft
M_∞	=	11.5	
α	=	36.2	deg
p_∞	=	1.0636	lb/ft2
T_∞	=	476.4	deg R
Re_L	=	2.9×10^6	

Figure 30 shows a plan-form view of the lower surface of the X-33, D Loft configuration with comparisons of the heating rate contours from the LATCH and LAURA codes. The LATCH results are shown on the bottom half of the figure and those from LAURA on the top. These calculations were for laminar flow and the wall temperature was assumed to be the radiation equilibrium wall temperature. The heating for this case is presented directly in terms of heat transfer rate (q_w) because the wall to total enthalpy ratio is relatively low (0.2 0.3) and the heating rate is relatively insensitive to wall temperature. From Fig. 30, it is observed that the two codes are in good qualitative agreement for this case. The heating rate contours in both the chine and canted-fin regions are very similar. Although the heating rate contours near the windward symmetry plane appear at first glance to be quite different, the heating in that region is nearly constant and the two calculations are actually in very good agreement.

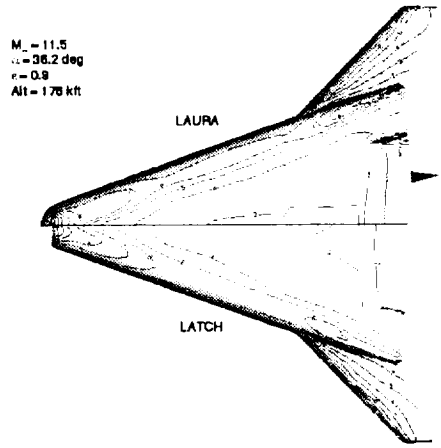

Fig. 30 Comparison of LATCH and LAURA heating rate predictions on the lower surface of X-33 in flight.

Heating distributions along the windward symmetry plane are presented in Fig. 31 and as well as lateral distributions at several axial stations, $x = 250$, 500, 550, 600, 650, and 700 inches, in Figs. 32 37, respectively. The lateral cut at $x = 250$ inches (Fig. 32) is on the forebody ahead of the canted fin. All of the remaining lateral cuts (Figs. 33 37) are downstream of the the canted-fin fuselage juncture (see Figs. 1 and 2). In general the LATCH and LAURA results are in very good agreement (± 10 percent) over most of the windward surface except in the chine region near the rear of the vehicle where the LATCH predictions are lower than LAURA by approximately 20 30 percent. The agreement between LATCH and LAURA at this flight condition is encouraging because it suggests that the LATCH code, which has a much faster turn around time than LAURA, can be used to predict flight heating rates for X-33 TPS design.

Concluding Remarks

Laminar and turbulent heating-rate calculations from an "engineering" code (LATCH) and laminar calculations from a "benchmark" Navier-Stokes code

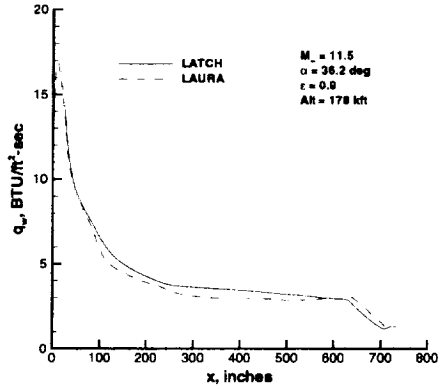

Fig. 31 Windward symmetry plane heating on the D-Loft configuration at $M_\infty = 11.5$, $\alpha = 36.2^o$, and $Re_L = 2.9x10^6$.

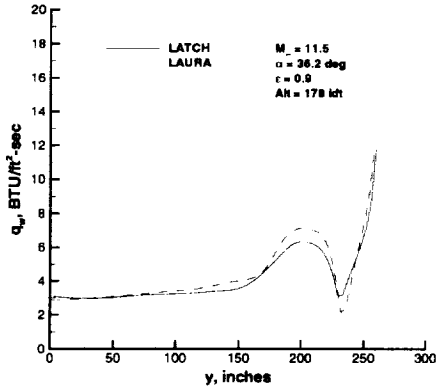

Fig. 34 Lateral heating distribution on the D-Loft configuration at $x = 550$ inches, $M_\infty = 11.5$, $\alpha = 36.2^o$, and $Re_L = 2.9x10^6$.

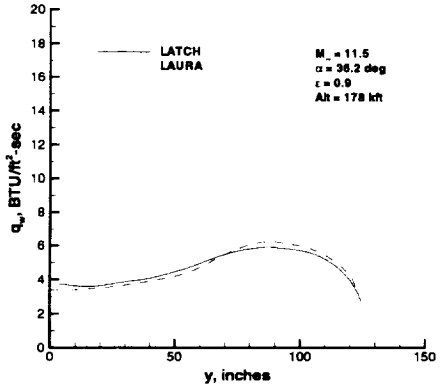

Fig. 32 Lateral heating distribution on the D-Loft configuration at $x = 250$ inches, $M_\infty = 11.5$, $\alpha = 36.2^o$, and $Re_L = 2.9x10^6$.

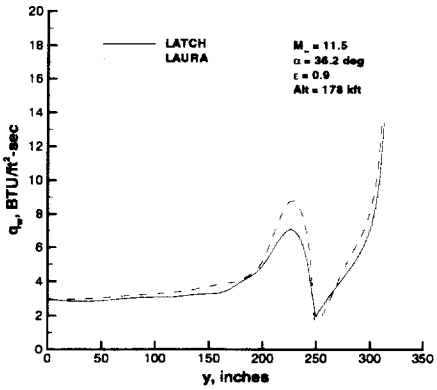

Fig. 35 Lateral heating distribution on the D-Loft configuration at $x = 600$ inches, $M_\infty = 11.5$, $\alpha = 36.2^o$, and $Re_L = 2.9x10^6$.

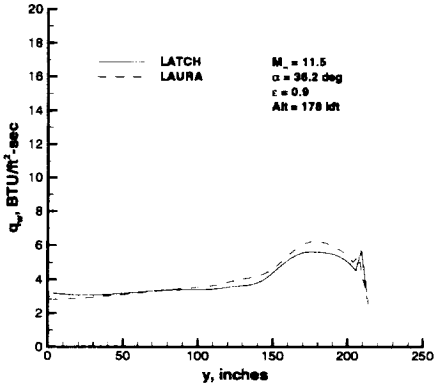

Fig. 33 Lateral heating distribution on the D-Loft configuration at $x = 500$ inches, $M_\infty = 11.5$, $\alpha = 36.2^o$, and $Re_L = 2.9x10^6$.

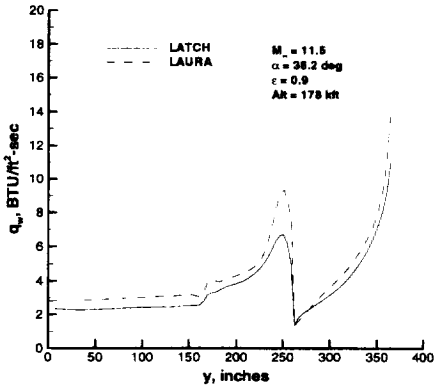

Fig. 36 Lateral heating distribution on the D-Loft configuration at $x = 650$ inches, $M_\infty = 11.5$, $\alpha = 36.2^o$, and $Re_L = 2.9x10^6$.

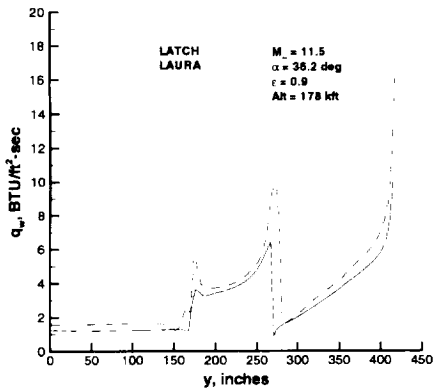

Fig. 37 Lateral heating distribution on the D-Loft configuration at x = 700 inches, M_∞ = 11.5, $\alpha = 36.2^o$, and $Re_L = 2.9x10^6$.

(LAURA) were compared with experimental wind-tunnel data obtained on several candidate configurations for the X-33 Phase II flight vehicle. The experimental data were obtained at a Mach number of 6 and a freestream Reynolds number ranging from approximately about 1 x 10^6 to 8 x 10^6/ft. Comparisons are presented along the windward symmetry plane and in a circumferential direction around the body at several axial stations at angles of attack from 20^o to 40^o. The experimental results include both laminar and turbulent flow.

For $\alpha = 40.^o$ the measured heating data along the windward symmetry plane exhibited a "non-laminar" behavior begining near $x/L = 0.1$ which caused the heating to increase above the laminar level long before "classical" transition to turbulent flow was observed and the departure from the laminar heating level increased with increasing Reynolds number. This behavior was not observed at the lower angles of attack (i. e. $\alpha = 20^o$ and 30^o). The predicted inviscid pressure distribution along the windward symmetry plane exhibited two over expansion and recompression regions, one near the nose ($x/L \approx 0.1$) and the other near the midpoint of the vehicle ($x/L \approx 0.45$). These recompressions were observed to increase in strength with angle of attack. Disturbances eminating from the recompression in the nose region may have disturbed the flow and contributed to the non-laminar behavior of the heating observed at the highest angle of attack.

When the flow was completely laminar, both codes predicted the measured heating along the windward symmetry plane reasonably well, generally within 10 percent; however, both codes under predicted the measured heating in the chine region, generally by 25 30 percent. When the flow was turbulent the LATCH code accurately predicted the measured heating rates within about 10-12 percent. Both codes were used to calculate heating rates over an X-33 vehicle at the peak heating point on the design trajectory and they were found to be in very good agreement except near the rear of the vehicle in the chine region.

Acknowledgments

C. J. Riley and W. L. Kleb (LaRC) computed some of the inviscid flowfield solutions used in the LATCH calculations presented in the paper. S. J. Alter (Lockheed Martin) developed the volume grids used in both the viscous and inviscid flowfield solutions. N. R. Merski (LaRC) assisted with interpretation of some of the thermographic phosphor data. B. R. Hollis and R. J. Nowak (LaRC) and Lisa Brilliant (Student, Purdue University) assisted with the reduction of the experimental heating data.

References

[1]Bekey, I., Powell, R., and Austin, R., "NASA Studies Access to Space," *Aerospace America*, May 1994, pp. 38–43.

[2]Cook, S. A., "X-33 Reusable Launch Vehicle Structural Technologies," AIAA Paper 97 10873, Nov. 1996.

[3]Freeman Jr., D. C., Talay, T. A., and Austin, R. E., "Reusable Launch Vehicle Technology Program," AIAA Paper IAF 96 V.4.01, Oct. 1996.

[4]Rodi, P., Green, M. G., and Zoby, E. V., "An Overview of the Aerothermal Design of the X-33 Vehicle," AIAA Paper 98 0863, Jan. 1998.

[5]Thompson, R. A., Hamilton II, H. H., Berry, S. A., Horvath, T. J., and Nowak, R. W., "Hypersonic Boundary Layer Transition for X-33 Phase II Vehicle," AIAA Paper 98 0867, Jan. 1998.

[6]Micol, J. R., "Aerodynamic/Aerothermodynamic Testing Capabilities at Langley Research Center: Aerothermodynamic Facilities Complex," AIAA Paper 95 2107, Jun. 1995.

[7]Buck, G. M., "Automated Thermal Mapping Techniques Using Chromatic Image Analysis," NASA TM 101554, Apr. 1989.

[8]Merski, Jr., N. R., "Reduction and Analysis of Phosphor Thermography Data With the IHEAT Software Package," AIAA Paper 98 00712, Jan. 1998.

[9]Buck, G. M. and Vasquez, P., "An Investment Ceramic Slip-Casting Technique for Net-Form, Precision, Detailed Casting of Ceramic Models," U. S. Pattent 5266252, Nov. 1993.

[10]Micol, J. R., "Aerothermodynamic Measurement and Prediction for a Modified Orbiter at Mach 6 and 10 in Air," AIAA Paper 91 1436, Jun. 1991.

[11]Gnoffo, P. A., "An Upwind-Biased, Point-Implicit Relaxation Algorithm for Viscous, Compressible Perfect-Gas Flows," NASA TP 2953, Feb. 1990.

[12]Gnoffo, P. A., "Point-Implicit Relaxation Strategies for Viscous, Hypersonic Flows," *Computational Methods in Hypersonic Aerothermodynamics*, edited by T. K. S. Murthy, Computational Mechanics Publications, Kluwer Academic Publishers, 1991, pp. 115 151.

[13]Cheatwood, F. M. and Gnoffo, P. A., "Users Manual for the Langley Aerthermodynamic Upwind Relaxation Algorithm (LAURA)," NASA TM 4674, Apr. 1996.

[14]Roe, P. L., "Approximate Riemann Solvers, Parameter Vectors, and Difference Schemes," *Journal of Computational Physics*, Oct. 1981, pp. 357 372.

[15]Yee, H. C., "On Symmetric and upwind TVD Schemes," NASA TM 88325, 1990.

[16]Gnoffo, P. A., Weilmuenster, K. J., and Alter, S. J., "Multiblock Analysis for Shuttle Orbiter Re-Entry Heating from Mach 24 to Mach 12," *Journal of Spacecraft and Rockets*, May-Jun. 1994, pp. 367 377.

[17]Gnoffo, P. A., "Code Calibration Program in Support of the Aeroassist Flight Experiment," *Journal of Spacecraft and Rockets*, Mar.-Apr. 1990, pp. 131-142.

[18]Hamilton, H. H., DeJarnette, F. R., and Weilmuenster, K. J., "Application of Axisymmetric Analog for Calculating Heating in Three-Dimensional Flows," *Journal of Spacecraft and Rockets*, Vol. 24, Jul.-Aug. 1987, pp. 296-302.

[19]Hamilton II, H. H., Greene, F. A., and DeJarnette, F. R., "Approximate Method for Calculating Heating Rates on Three-Dimensional Vehicles," *Journal of Spacecraft and Rockets*, Vol. 31, No. 3, May-Jun. 1994, pp. 345-354.

[20]Cooke, J. C., "An Axially Symmetric Analogue for General Three-Dimensional Boundary Layers," Reports and Memoranda 3200, 1961.

[21]Zoby, E. V., Moss, J. N., and K., S., "Approximate Convective Heating Analysis for Hypersonic Flows," *Journal of Spacecraft and Rockets*, Vol. 18, No. 1, Jan. 1981, pp. 64-70.

[22]Candler, G. V., Wright, M. J., and McDonald, J. D., "Data-Parallel Lower-Upper Relaxation Method for Reacting Flows," *AIAA Journal*, Vol. 32, No. 12, Dec. 1994, pp. 2380-2386.

[23]Riley, C. J., Kleb, W. L. K., and Alter, S. J., "Aeroheating Predictions for X-34 Using an Inviscid-Boundary Layer Method," AIAA Paper 98–0880, Jan. 1998.

[24]Fay, J. A. and Riddell, F. R., "Theory of Stagnation Point Heat Transfer in Dissociated Air," *Journal of the Aeronautical Sciences*, Vol. 25, No. 2, Feb. 1958, pp. 73–85.

[25]Berry, S. A., Bouslog, S. A., Brauckmann, G. J., and Caram, J. M., "Boundary Layer Transition Due to Isolated Roughness: Shuttle Results from LaRC 20-Inch Mach 6 Tunnel," AIAA Paper 97-0273, Jan. 1997.